The International Archives of the Photogrammetry, Remote Sensing and Spatial Information Sciences, Volume XLVIII-2/W7-2024
Optical 3D Metrology (O3DM), 12–13 December 2024, Brescia, Italy

Eccentricity Correction Methods for Circular Targets in Perspective Projection

Frank Liebold, Hans-Gerd Maas

Institute of Photogrammetry and Remote Sensing, Technische Universität Dresden, Germany -
(frank.liebold, hans-gerd.maas)@tu-dresden.de

Technical Commission II

Keywords: Circular Target, Eccentricity, Perspective Projection, Bundle Adjustment, Scale, Precision.

Abstract

In a perspective projection, a circular target appears as an ellipse for an oblique view. The ellipse center as a result of the image coordinate measurement differs from the projection of the circle center. This discrepancy is called eccentricity and may lead to systematic errors. This contribution discusses four different correction methods that can be applied on the observation or the model side. The last method includes the determination of the circle radius and thus also offers a possibility to define the scale. The correction procedures are applied in an experiment with high eccentricities where the remaining error is significantly reduced. In another experiment, the precision and accuracy of the scale definition is investigated.

1. Introduction

In photogrammetry, circular targets are often used for high accuracy 3D object point coordinate determination applications due to the good contrast and well established detection methods. In non-perpendicular views, a circle appears as an ellipse when it is mapped in a perspective projection. Mathematically, this can be seen as a conic section of an oblique cone. In this projection, the center of the ellipse differs from the projection of the circle center. This deviation is called eccentricity, and it will lead to systematic measurement errors if the effect is not taken into account (Lenz and Fritsch, 1988). The error can be minimized by the usage of small target sizes, nearly perpendicular viewing directions and large target to camera distances. (Dold, 1996) proposed a simple expression for the eccentricity using a 2D scheme. He also computed a simulation to analyze the influence on the parameter estimation in a bundle adjustment. He observed a slight influence on the residuals and the object coordinates, but a higher influence on the interior and exterior orientation parameters. (Heikkilä and Silvén, 1997) presented a four-step calibration procedure including a direct linear transformation and a compensation of the eccentricity of circular features. A 3D extension to Dold's expression was given by (Ahn et al., 1999). They also discussed the eccentricity correction with known radii and normals of the circles. (Otepka and Fraser, 2004) proposed an extended bundle adjustment which took the eccentricity into account and where the implicit parameters of the image ellipses were used as observations and circle radii and normals are introduced as unknowns. (Wrobel, 2012) also considered the perspective projections of circular targets and discussed different approaches for the mathematical description. Another approximation of the eccentricity correction can be obtained by the usage of targets with concentric circles shown by (He et al., 2012) based on the idea of (Kim et al., 2002). (He et al., 2012) showed that the remaining approximation error is neglectable. (Luhmann, 2014) computed the projections of simulated circle contour points and performed an ellipse fit with the projected points to get the ellipse center as well as the eccentricity. (Matsuoka and Maruyama, 2016) proposed a complex calculation rule to compute the ellipse parameters from a given circle center, radius and normal as well as interior and exterior orientation.

The article at hand describes the eccentricity mathematically and provides an extension to the collinearity equations for circles that the can be used easily (less complex than (Ahn et al., 1999) and (Matsuoka and Maruyama, 2016)), which will be shown in Section 2. Then in Section 3, four possible correction methods are discussed. In the fourth correction procedure, the radii of the circles are part of the model that can be introduced as unknowns or, secondly, as constants in a bundle adjustment. This means that they also can be used for the definition of the scale which is considered in Section 5. The article ends with a conclusion.

2. Mathematical Description of the Eccentricity

2.1 Computation of the Ellipse Center

(Dold, 1996) shows in his Eq. 2 a calculation for a 2D scheme that cannot be used directly to compute the error in 3D in general. Based on his idea, the formula will be extended to 3D similar to (Ahn et al., 1999). First, the circle center $\vec{X}_C$ and its normal $\vec{n}$ (with $||\vec{n}|| = 1$) are transformed into the camera frame:

$$\begin{aligned} \vec{n}_{cam} &= \mathbf{R}^T \cdot \vec{n} \\ \vec{X}_{C,cam} &= \mathbf{R}^T \cdot (\vec{X}_C - \vec{X}_{projC}) \end{aligned} \tag{1}$$

where $\mathbf{R}$ = rotation matrix of the camera
$\vec{X}_{projC}$ = projection center of the camera
$\vec{X}_{C,cam}$ = circle center in camera frame
$\vec{n}_{cam}$ = circle normal in camera frame

To compute the coordinates of the projected circle center, Dold's method is applied to a special diameter. It is the diameter which is the intersection of the circle and the plane containing the circle center $\vec{X}_{C,cam}$, the circle normal $\vec{n}_{cam}$ and the optical axis direction (z direction of the camera frame $(\,0\;0\;1\,)^T$). The illustration in Fig. 1 shows the projection of a circle (in magenta) into an image where it appears as an ellipse (cyan). The diameter of interest is also depicted in orange.

The direction vector $\vec{h}$ of the diameter in the camera frame is computed by applying the cross product which is valid for $\vec{n}_{cam} \neq \begin{pmatrix}0 & 0 & 1\end{pmatrix}^T$:

$$\vec{h} = \vec{n}_{cam} \times \frac{\vec{n}_{cam} \times \begin{pmatrix}0\\0\\1\end{pmatrix}}{||\vec{n}_{cam} \times \begin{pmatrix}0\\0\\1\end{pmatrix}||} = \frac{\begin{pmatrix} n_{cam,x} \cdot n_{cam,z} \\ n_{cam,y} \cdot n_{cam,z} \\ -n_{cam,x}^2 - n_{cam,y}^2 \end{pmatrix}}{\sqrt{n_{cam,x}^2 + n_{cam,y}^2}} \quad (2)$$

Thus, the opposite circle points on this diameter are:

$$\vec{X}_{C \pm R,cam} = \vec{X}_{C,cam} \pm R_C \cdot \vec{h} \quad (3)$$

where R_C = radius of circle

After this, the circle points $\vec{X}_{C+R,cam}$ and $\vec{X}_{C-R,cam}$ are projected into the image:

$$\vec{x}_{C \pm R,cam} = \vec{x}_p - \frac{c}{Z_{C \pm R,cam}} \cdot \begin{pmatrix} X_{C \pm R,cam} \\ Y_{C \pm R,cam} \end{pmatrix} \quad (4)$$

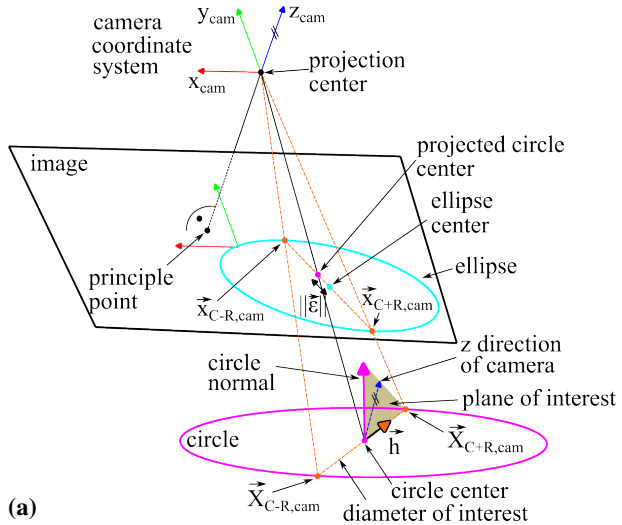

(a)

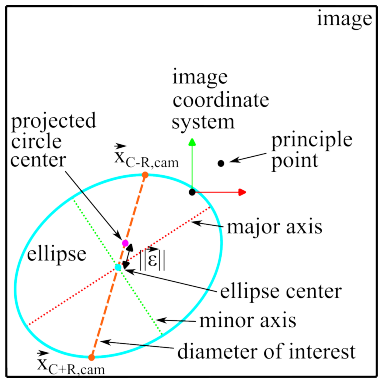

(b)

Figure 1. Projection of a circle (magenta) into an image results as ellipse (cyan). Projected circle center differs from ellipse center with $||\vec{\epsilon}||$. The diameter of interest is colored orange. **(a)** shows the 3D projection, **(b)** shows the corresponding image.

The ellipse center $\vec{x}_{ell,c}$ is then obtained by averaging the projected circle points at the ends of the diameter:

$$\vec{x}_{ell,c} = \frac{1}{2} \cdot (\vec{x}_{C+R,cam} + \vec{x}_{C-R,cam}) \quad (5)$$

Inserting and simplifying yields

$$x_{ell,c} = x_p - c \cdot \frac{X_{C,cam} \cdot Z_{C,cam} + R_C^2 \cdot n_{cam,x} \cdot n_{cam,z}}{Z_{C,cam}^2 - R_C^2 \cdot (n_{cam,x}^2 + n_{cam,y}^2)}$$
$$y_{ell,c} = y_p - c \cdot \frac{Y_{C,cam} \cdot Z_{C,cam} + R_C^2 \cdot n_{cam,y} \cdot n_{cam,z}}{Z_{C,cam}^2 - R_C^2 \cdot (n_{cam,x}^2 + n_{cam,y}^2)} \quad (6)$$

where $\begin{pmatrix}x_{ell,c}, y_{ell,c}\end{pmatrix}^T$ = ellipse center in image
c = principle distance
x_p, y_p = principle point coordinates

Eq. 6 is simple to use and shows how to compute the ellipse center coordinates with a given exterior image orientation, inner orientation as well as circle center, radius and normal. In the following, it is called extended collinearity equation for circles.

If $R_c = 0$ (circle = point) or if $\vec{n}_{cam} = \begin{pmatrix}0 & 0 & 1\end{pmatrix}^T$ (perpendicular view), Eq. 6 will lead to the collinearity equations for points (standard pinhole model), resulting in the projected circle center coordinates $\begin{pmatrix}x_{C,c}, y_{C,c}\end{pmatrix}^T$:

$$x_{C,c} = x_p - c \cdot \frac{X_{C,cam}}{Z_{C,cam}}$$
$$y_{C,c} = y_p - c \cdot \frac{Y_{C,cam}}{Z_{C,cam}} \quad (7)$$

2.2 Eccentricity Calculation

The eccentricity error is computed by the difference of the ellipse center and the projected circle center:

$$\vec{\epsilon} = \begin{pmatrix} x_{C,c} \\ y_{C,c} \end{pmatrix} - \begin{pmatrix} x_{ell,c} \\ y_{ell,c} \end{pmatrix} \quad (8)$$

Eq. 8 can now be used to calculate the eccentricity for different scenarios. An example is demonstrated in Fig. 2 where a planar grid of 5×5 circles with 20 mm radius is defined with a grid size of 60 mm. The assumed projection center of the camera (2048×2048 px, pixel size: 5.5 µm, focal length: 12 mm) has a horizontal distance of 120 mm and vertical distance of 330 mm to the centroid. The optical axis points to the centroid and has an angle of $\approx 20°$ to the plane's normal. The computed ellipses are plotted and the eccentricities are shown as a vector field. In this case the deviations reach values of up to 3.3 px.

2.3 Eccentricity Approximation

In addition to Sec. 2.2, this section shows an approximation of the eccentricity because it will be applied in a later section. The denominator in Eq. 6 can be transformed with the assumption $Z_{C,cam}^2 \gg R_C^2$:

$$Z_{C,cam}^2 - R_C^2 \cdot (n_{cam,x}^2 + n_{cam,y}^2) \approx Z_{C,cam}^2 \quad (9)$$

Eq. 6 becomes simplified as follows where the fraction is split:

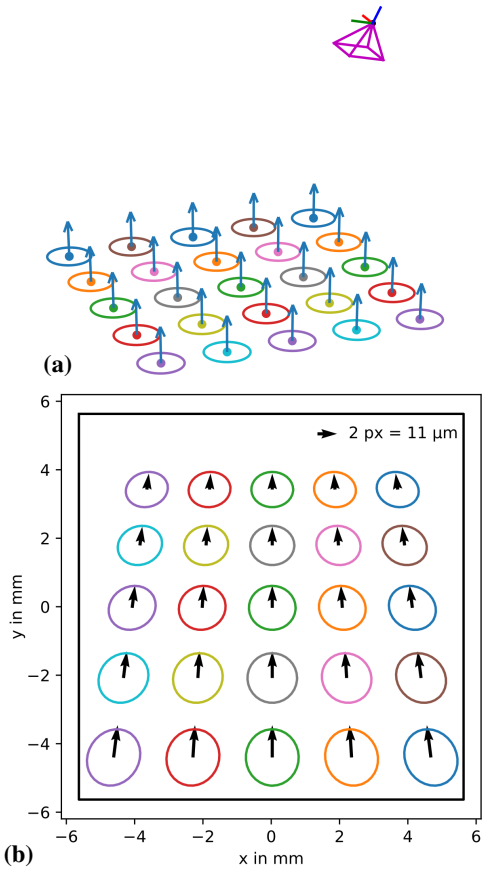

Figure 2. Example for eccentricity: **(a)** grid of circles (with centers and normals) and camera orientation, **(b)** image with projected ellipses and eccentricities as vector field.

$$
\begin{aligned}
x_{ell,c} &\approx \underbrace{x_p - c \cdot \frac{X_{C,cam}}{Z_{C,cam}}}_{=x_{C,c}} - \underbrace{\frac{c \cdot R_C^2 \cdot n_{cam,x} \cdot n_{cam,z}}{Z_{C,cam}^2}}_{=e_x \approx \epsilon_x} \\
y_{ell,c} &\approx \underbrace{y_p - c \cdot \frac{Y_{C,cam}}{Z_{C,cam}}}_{=y_{C,c}} - \underbrace{\frac{c \cdot R_C^2 \cdot n_{cam,y} \cdot n_{cam,z}}{Z_{C,cam}^2}}_{=e_y \approx \epsilon_y}
\end{aligned}
\tag{10}
$$

The left parts of the right hand side are the coordinates of the projected circle center $\vec{x}_{c,c}$ and the right parts are summarized in $e_x \approx \epsilon_x$ and $e_y \approx \epsilon_y$ that represents an approximation for the eccentricity.

$$
\vec{\epsilon} \approx \vec{e} = \frac{c \cdot R_C^2 \cdot n_{cam,z}}{Z_{C,cam}^2} \cdot \begin{pmatrix} n_{cam,x} \\ n_{cam,y} \end{pmatrix} \tag{11}
$$

The approximation in Eq. 11 shows the dependencies of the eccentricity $e \approx \epsilon$.

- e is proportional to the principle distance: $e \sim c$,
- e is proportional to the squared radius: $e \sim R_C^2$,
- e is inversely proportional to the squared z coordinate in the camera frame: $e \sim Z_{C,cam}^{-2}$,
- e can be eliminated for a perpendicular view: $n_{cam,x} = n_{cam,y} = 0$.

3. Eccentricity Correction Methods

This section shows four different correction methods for the eccentricity. The first two are applied on the observation side and the last two on the model side. An observation-side correction means that an offset is added to the observed ellipse center to eliminate the systematic error when using the pinhole model. In contrast to this, a model-side correction modifies the pinhole model so that the output of the mapping process is the ellipse center instead of the projected circle center.

3.1 Image Coordinate Correction with Radius and Normal

The correction in this section is applied on the observation side using Eq. 11 (or Eq. 8) where the normal directions and the radii of the circular targets must be known. In case of a space resection or a bundle adjustment, the interior and exterior orientations can be obtained without eccentricity correction in a first step. After this, the corrections are computed with the results of step one. The corrections can also be updated in further iterations. This method is suitable for special cases such as planar test fields, where the normals can be obtained by a plane fit. Another possibility is the use of a test field with target groups of at least three coplanar targets so that the normals can be calculated as triangle normals that was also proposed by (Ahn et al., 1999).

3.2 Correction with Concentric Circle Targets

(He et al., 2012) proposed a procedure where the eccentricity can be corrected approximately with the help of the measurement of the ellipse centers of two concentric circles and the knowledge of their radii. The correction is also derived here using the approximation of Sec. 2.3. For concentric circles, Eq. 11 only differs in the radii $R_{c,1}$ and $R_{c,2}$, and the following system can be set up:

$$
\begin{aligned}
\vec{x}_{ell,c,1} &\approx \vec{x}_{C,c} - \vec{e}_1 \\
\vec{x}_{ell,c,2} &\approx \vec{x}_{C,c} - \vec{e}_2 \\
\frac{e_{x,1}}{e_{x,2}} = \frac{e_{y,1}}{e_{y,2}} &= \frac{R_{C,1}^2}{R_{C,2}^2} \quad \text{or} \quad \vec{e}_1 = \frac{R_{C,1}^2}{R_{C,2}^2} \cdot \vec{e}_2
\end{aligned}
\tag{12}
$$

The third equation is inserted in the first and then, the first two equations are solved for $\vec{x}_{c,c}$. The solution is

$$
\vec{x}_{C,c} \approx \vec{x}_{ell,c,1} + \frac{\vec{x}_{ell,c,2} - \vec{x}_{ell,c,1}}{1 - (\frac{R_{C,2}}{R_{C,1}})^2} \tag{13}
$$

With Eq. 13, the projected circle center can be estimated with the two ellipse center measurements and the knowledge of the ratio of the radii. The right term in Eq. 13 represents the approximation for the eccentricity correction for the first ellipse measurement, see Eq. 14. Note that the correction can be computed without the knowledge of the circle normal.

$$
\vec{\epsilon}_1 \approx \vec{e}_1 = \frac{\vec{x}_{ell,c,2} - \vec{x}_{ell,c,1}}{1 - (\frac{R_{C,2}}{R_{C,1}})^2} \tag{14}
$$

Fig. 3 shows an example with two ellipse measurements (red and green) and the corrected point (blue cross) that represents the projected circle center. In the center of the circular target, a black cross was printed that can also be seen.

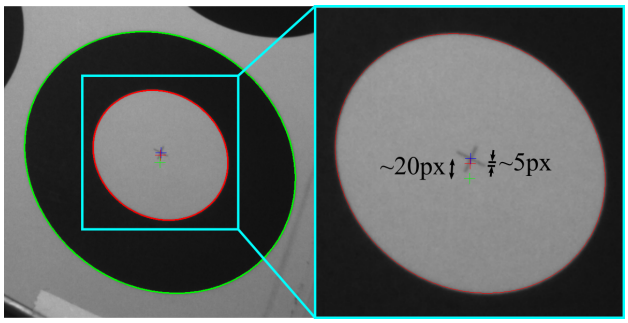

Figure 3. Eccentricity correction with ellipse measurements of two concentric circles, inner ellipse and their center in red, outer ellipse in green, corrected coordinate in blue.

3.3 Model-side Correction with Normal and Radius

Another way to take the eccentricity into account is the adaption of the pinhole model. For this correction on the model side, the standard pinhole model is replaced with Eq. 1 and Eq. 6 so that the ellipse center from the circle projection is computed directly. Just like in Sec. 3.1, the circle normal and radius have to be known and there are only special cases, where the normals can be estimated, see Sec. 3.1.

3.4 Extended Bundle Adjustment

The fourth procedure, that takes the eccentricity into account, follows the idea of an extended bundle adjustment similar to the method of (Otepka and Fraser, 2004). They used the implicit ellipse parameters of the image measurements to obtain the circle center coordinates, the normal and the radius as unknowns in a bundle adjustment. In the article at hand, the extended bundle adjustment is performed in a different way where in addition to the ellipse center coordinates, the semi-minor and semi-major axes lengths are used as observations. The lens distortion can also be considered. In contrast to Section 3.3, this algorithm is not limited to special cases because the circle normals as well as the circle radii belong to the unknowns that are computed in the bundle adjustment so that only initial values have to be obtained.

With the method of (Matsuoka and Maruyama, 2016), the coefficients of the implicit ellipse form are computed that fulfill the following equation for the image ellipse contour points (x_Q, y_Q) (Eq. 15, Eq. 16, Eq. 17 and Eq. 18 adopted from (Matsuoka and Maruyama, 2016) and partly adapted).

$$\begin{aligned} &p_{xx} \cdot x_Q^2 + p_{yy} \cdot y_Q^2 + p_{cc} \cdot c^2 + 2 \cdot p_{xy} \cdot x_Q \cdot y_Q \\ &+2 \cdot p_{xc} \cdot x_Q \cdot c + 2 \cdot p_{yc} \cdot y_Q \cdot c = 0 \end{aligned} \tag{15}$$

The coefficients are calculated using the normal and the circle center in the camera frame after applying Eq. 1:

$$\begin{aligned} p_{xx} &= (n_{cam,x}^2 + n_{cam,y}^2) \cdot Y_{C,cam}^2 \\ &+ 2 \cdot n_{cam,y} \cdot n_{cam,z} \cdot Y_{C,cam} \cdot Z_{C,cam} \\ &+ (n_{cam,x}^2 + n_{cam,z}^2) \cdot Z_{C,cam}^2 - n_{cam,x}^2 \cdot R_C^2 \\ p_{yy} &= (n_{cam,x}^2 + n_{cam,y}^2) \cdot X_{C,cam}^2 + \\ &+ 2 \cdot n_{cam,x} \cdot n_{cam,z} \cdot X_{C,cam} \cdot Z_{C,cam} \\ &(n_{cam,y}^2 + n_{cam,z}^2) \cdot Z_{C,cam}^2 - n_{cam,y}^2 \cdot R_C^2 \\ p_{cc} &= (n_{cam,x}^2 + n_{cam,z}^2) \cdot X_{C,cam}^2 \\ &+ 2 \cdot n_{cam,x} \cdot n_{cam,y} \cdot X_{C,cam} \cdot Y_{C,cam} \\ &+ (n_{cam,y}^2 + n_{cam,z}^2) \cdot Y_{C,cam}^2 - n_{cam,z}^2 \cdot R_C^2 \\ p_{xy} &= n_{cam,x} \cdot n_{cam,y} \cdot (Z_{C,cam}^2 - R_C^2) \\ &- n_{cam,x} \cdot n_{cam,z} \cdot Y_{C,cam} \cdot Z_{C,cam} \\ &- n_{cam,y} \cdot n_{cam,z} \cdot X_{C,cam} \cdot Z_{C,cam} \\ &- (n_{cam,x}^2 + n_{cam,y}^2) \cdot X_{C,cam} \cdot Y_{C,cam} \\ p_{xc} &= n_{cam,x} \cdot n_{cam,z} \cdot (R_C^2 - Y_{C,cam}^2) \\ &+ n_{cam,x} \cdot n_{cam,y} \cdot Y_{C,cam} \cdot Z_{C,cam} \\ &+ n_{cam,y} \cdot n_{cam,z} \cdot X_{C,cam} \cdot Y_{C,cam} \\ &+ (n_{cam,x}^2 + n_{cam,z}^2) \cdot X_{C,cam} \cdot Z_{C,cam} \\ p_{yc} &= n_{cam,y} \cdot n_{cam,z} \cdot (R_C^2 - X_{C,cam}^2) \\ &+ n_{cam,x} \cdot n_{cam,y} \cdot X_{C,cam} \cdot Z_{C,cam} \\ &+ n_{cam,x} \cdot n_{cam,z} \cdot X_{C,cam} \cdot Y_{C,cam} \\ &+ (n_{cam,y}^2 + n_{cam,z}^2) \cdot Y_{C,cam} \cdot Z_{C,cam} \end{aligned} \tag{16}$$

The implicit ellipse parameters are then transformed to the parametric form. The ellipse center coordinates are expressed in Eq. 17. Note that inserting Eq. 16 into Eq. 17 and simplifying leads to Eq. 6.

$$\begin{aligned} x_{ell,c} &= x_p - c \cdot \frac{p_{yy} \cdot p_{xc} - p_{xy} \cdot p_{yc}}{p_{xx} \cdot p_{yy} - p_{xy}^2} \\ y_{ell,c} &= y_p - c \cdot \frac{p_{xx} \cdot p_{yc} - p_{xy} \cdot p_{xc}}{p_{xx} \cdot p_{yy} - p_{xy}^2} \end{aligned} \tag{17}$$

The semi-major and semi-minor axes and the inclination are

$$\begin{aligned} w &= ((x_{ell,c} - x_p) \cdot p_{xc} + (y_{ell,c} - y_p) \cdot p_{yc} + p_{cc} \cdot c) \cdot c \\ \hat{a} &= \sqrt{\frac{-2 \cdot w}{p_{xx} + p_{yy} - \sqrt{(p_{xx} - p_{yy})^2 + 4 \cdot p_{xy}^2}}} \\ \hat{b} &= \sqrt{\frac{-2 \cdot w}{p_{xx} + p_{yy} + \sqrt{(p_{xx} - p_{yy})^2 + 4 \cdot p_{xy}^2}}} \\ \varphi &= \frac{1}{2} \cdot arctan2(2 \cdot p_{xy}, p_{yy} - p_{xx}) \end{aligned} \tag{18}$$

For applying lens distortion correction, first, the four points at main axes are computed:

$$\begin{aligned} x_{ell,c\pm a} &= x_{ell,c} \pm \cos(\varphi) \cdot \hat{a} \\ y_{ell,c\pm a} &= y_{ell,c} \pm \sin(\varphi) \cdot \hat{a} \\ x_{ell,c\pm b} &= x_{ell,c} \mp \sin(\varphi) \cdot \hat{b} \\ y_{ell,c\pm b} &= y_{ell,c} \pm \cos(\varphi) \cdot \hat{b} \end{aligned} \tag{19}$$

After this, lens distortion correction is computed for the ellipse center $\vec{x}_{ell,c}$ and the four points at the ends of the main axes

$\vec{x}_{ell,c\pm a}$ and $\vec{x}_{ell,c\pm b}$ with the model of (Brown, 1971) represented by the function $distortionCorrection$:

$$\begin{aligned} \Delta\vec{x}_{ell,c,dist} &= distortionCorrection(\vec{x}_{ell,c}) \\ \Delta\vec{x}_{ell,c\pm a,dist} &= distortionCorrection(\vec{x}_{ell,c\pm a}) \\ \Delta\vec{x}_{ell,c\pm b,dist} &= distortionCorrection(\vec{x}_{ell,c\pm b}) \end{aligned} \quad (20)$$

The lens distortion corrected semi-major and semi-minor axes lengths are then computed as the half distances between the ellipse points at the axes. For the ellipse center, it is obvious.

$$\vec{x}_{ell,c,dist} = \vec{x}_{ell,c} + \Delta\vec{x}_{ell,c,dist} \quad (21)$$

$$a_{dist} = \frac{1}{2} \cdot ||\vec{x}_{ell,c+a} + \Delta\vec{x}_{ell,c+a,dist} - \vec{x}_{ell,c-a} - \Delta\vec{x}_{ell,c-a,dist}|| \quad (22)$$

$$b_{dist} = \frac{1}{2} \cdot ||\vec{x}_{ell,c+b} + \Delta\vec{x}_{ell,c+b,dist} - \vec{x}_{ell,c-b} - \Delta\vec{x}_{ell,c-b,dist}|| \quad (23)$$

All in all, the ellipse center and the main axes can be computed as a function (Eq. 1 and Eq. 16 to Eq. 23) of the exterior and interior orientation as well as the circle parameters:

$$\begin{pmatrix} x_{ell,c,dist} \\ y_{ell,c,dist} \\ a_{dist} \\ b_{dist} \end{pmatrix} = \vec{f}\begin{pmatrix} \vec{X}_{projC}, \mathbf{R}, c, x_p, y_p, \vec{X}_C, R_C, \vec{n}, \\ \textit{lens distortion coefficients} \end{pmatrix} \quad (24)$$

The measurement of the ellipse center and the main axes are considered as observations so that the parameters in the function can be estimated in a bundle adjustment by minimizing the residuals between the measurements and the computed values of Eq. 24. The Jacobian matrix can be calculated with numerical derivations by central differences applied to Eq. 24.

4. Experimental Tests

The procedures of Section 3 has been applied and compared in an experiment with a planar test field of concentric circles of different sizes.

4.1 Experimental Setup

A planar test field of 20 concentric circles was created with a vector graphics software (Fig. 4). Tab. 1 shows the coordinates as well as the small and large radii. The Z coordinate of the circles was $Z_C = 0$ so that the circle normals were $(\,0\;0\;1\,)^T$.

A bundle of twelve images was recorded with an AVT Mako G-419C camera (2048 × 2048 px and 5.5 µm pixel size) with a lens of 12 mm focal length. The image orientations are shown in Fig. 5.

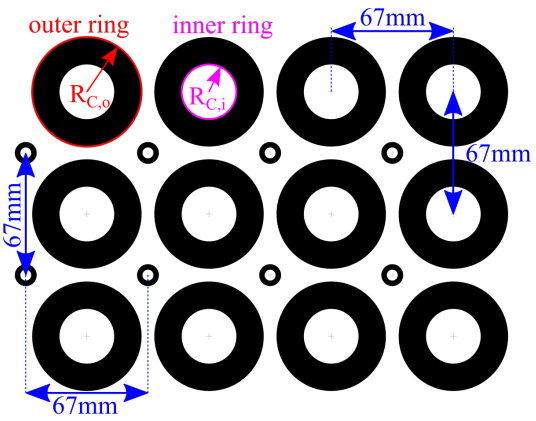

Figure 4. Test field of circular targets of different size.

X_C in mm	Y_C in mm	$R_{C,i}$ in mm	$R_{C,o}$ in mm
0	0	15	30
0	67	15	30
0	134	15	30
67	0	15	30
67	67	15	30
67	134	15	30
134	0	15	30
134	67	15	30
134	134	15	30
201	0	15	30
201	67	15	30
201	134	15	30
33.5	33.5	3	6
33.5	100.5	3	6
100.5	33.5	3	6
100.5	100.5	3	6
167.5	33.5	3	6
167.5	100.5	3	6
234.5	33.5	3	6
234.5	100.5	3	6

Table 1. Circle coordinates and small and large radii of the planar test field.

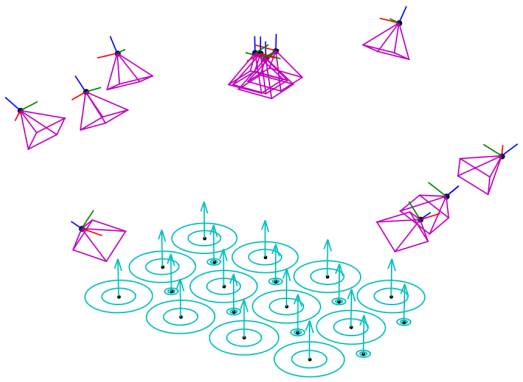

Figure 5. Experimental setup. Image orientations and planar test field of concentric circles with centers and normals.

Initial values for the exterior orientation in Fig. 5 were obtained by space resections of each image and assuming an ideal distortion-free camera with a principle distance of 12 mm. The eccentricities reached values of up to 6 px (for inner rings, 23 px for outer rings) in the oblique images (computed with Eq. 14).

4.2 Simulation

To check the algorithms and to estimate the influence of the eccentricity, simulations were performed with the different models. For each image, the image coordinates of the ellipse centers were computed with Eq. 6 inserting the initial values of the exterior orientation (Fig. 5) and assuming a distortion-free lens with 12 mm principle distance. These image coordinates were then used as observations without additional artificial noise for a bundle adjustment (BA) with the different procedures shown in Sec. 3. The BA was computed as a free net adjustment where all circle centers were unknowns as well as the exterior and interior orientation (including lens distortion correction). Seven constraints were introduced for the free net adjustment:

$$\sum_i d\vec{X}_{C,i} = \sum_i \vec{X}_{C,i} \times d\vec{X}_{C,i} = \vec{0} \qquad (25)$$
$$\sum_i \vec{X}_{C,i}^T \cdot d\vec{X}_{C,i} = 0$$

where $\vec{X}_{C,i}$ = center of the ith circle
$d\vec{X}_{C,i}$ = correction vector for $\vec{X}_{C,i}$ from BA

Eleven different scenarios were performed that are listed in Table 2. For five cases, only the inner rings of concentric circles were used as input, for five other cases, only the outer rings of concentric circles. Scenario M_7 works with the corrected image coordinates calculated with both rings. In case of M_{10} and M_{11} (Sec. 3.4), the circles normals and radii were also introduced as unknowns.

ID	Model	Input
M_1	Standard pinhole model w/o ecc. corr.	inner rings
M_2	Standard pinhole model w/o ecc. corr.	outer rings
M_3	Obs.-side corr. of Sec. 3.1 with Eq. 11	inner rings
M_4	Obs.-side corr. of Sec. 3.1 with Eq. 11	outer rings
M_5	Obs.-side corr. of Sec. 3.1 with Eq. 8	inner rings
M_6	Obs.-side corr. of Sec. 3.1 with Eq. 8	outer rings
M_7	Observation-side correction of Sec. 3.2	both rings
M_8	Model-side correction of Sec. 3.3	inner rings
M_9	Model-side correction of Sec. 3.3	outer rings
M_{10}	Model-side correction of Sec. 3.4	inner rings
M_{11}	Model-side correction of Sec. 3.4	outer rings

Table 2. Scenarios of bundle adjustments.

The following quantities are used to evaluate the different methods:

- RMS_{BA}: RMS of the residuals of the image coordinates of the ellipse centers after BA to show the influence on the model fit,
- c: estimated principle distance to show the influence on the interior orientation,
- RMS_{ST-C}: RMS of the residuals of the parameter estimation of a similarity transformation between the a priori and a posteriori circle centers to show the influence on the circle centers,
- RMS_{ST-P}: RMS of the residuals of the parameter estimation of a similarity transformation between the a priori and a posteriori projection centers to show the influence on the exterior orientation.

Table 3 shows results of the different scenarios. The standard pinhole model without eccentricity correction (M_1, M_2) showed the highest residuals of the image coordinates. The outer rings M_2 resulted in the highest deviations as the four times higher RMS_{BA} compared to the inner rings M_1 with the halved radii. The effect on the interior orientation is revealed by the difference to the a priori principle distance of 12 mm. The RMS_{ST-C} of M_1 and M_2 was four times smaller than RMS_{ST-P} so that there was a higher influence on the exterior orientation than on the circle coordinates. When the observation-side correction with the approximated eccentricity was applied (M_3, M_4), the RMS_{BA} was halved and the other deviations were even smaller than the half. Thus, the error could not be fully removed. The exact correction terms (M_5, M_6) should be preferred . They, as well as the other correction models, resulted in zero deviations that showed that the models work. Note, that no additional noise has been added. Only M_7 shows a slightly non-zero RMS_{BA} of 0.002 px due to the approximation, but much smaller than M_3 and M_4. Some remaining errors of M_3 and M_4 seem to be eliminated by the coordinate difference calculation in M_7.

	RMS_{BA} in px	c in mm	RMS_{ST-C} in mm	RMS_{ST-P} in mm
M_1	0.169	12.04	0.15	0.60
M_2	0.668	12.14	0.60	2.49
M_3	0.089	12.00	0.02	0.16
M_4	0.359	12.05	0.08	0.95
M_5	0.000	12.00	0.00	0.00
M_6	0.000	12.00	0.00	0.00
M_7	0.002	12.00	0.00	0.00
M_8	0.000	12.00	0.00	0.00
M_9	0.000	12.00	0.00	0.00
M_{10}	0.000	12.00	0.00	0.00
M_{11}	0.000	12.00	0.00	0.00

Table 3. BA results of different models for simulations with 12 larger and 8 smaller concentric circles.

Different results were be obtained when only the first twelve targets of equal size in Table 1 with the larger radii were used. The results are revealed in Table 4. The deviations of the standard pinhole model without eccentricity correction (M_1, M_2) were significantly smaller. The other scenarios behave similar to the first simulation but there was an underestimation of c without eccentricity correction. The systematic eccentricity errors seem to be much better compensated by the exterior orientation parameters, as can also be seen from Fig. 2.

	RMS_{BA} in px	c in mm	RMS_{ST-C} in mm	RMS_{ST-P} in mm
M_1	0.022	11.99	0.01	0.19
M_2	0.089	11.95	0.02	0.78
M_3	0.006	11.98	0.00	0.09
M_4	0.026	11.93	0.00	0.37
M_5	0.000	12.00	0.00	0.00
M_6	0.000	12.00	0.00	0.00
M_7	0.001	12.00	0.00	0.00
M_8	0.000	12.00	0.00	0.00
M_9	0.000	12.00	0.00	0.00
M_{10}	0.000	12.00	0.00	0.00
M_{11}	0.000	12.00	0.00	0.00

Table 4. BA results of different models with simulated image coordinates for the 12 larger equal sized concentric circles.

It can be concluded that the eccentricity error of circular targets on a planar test field should lead to much higher deviations when the targets are not of the same size. In the present case with a planar target field, this can be explained by correlations

between target eccentricity parameters and camera exterior orientation parameters. This, however, only holds in case of a planar target field and can thus not be generalized.

4.3 Bundle Adjustment with Real Image Measurements

In this section, the same scenarios of the simulations from the prior section were performed with the real image measurements. The star operator (Luhmann et al., 2020) was used to measure the image ellipses. The results of the different BAs (as free net adjustments) are shown in Table 5 for the 20 concentric circles of Fig. 5. Again, the RMS of the image ellipse center residuals RMS_{BA} after BA is shown as well as the principle distance and the RMS of the residuals of the parameter estimation of a similarity transformation between the a priori and a posteriori circle centers RMS_{ST-C}. The a priori circle centers can be assumed as target values neglecting printing errors.

There is a high degree of consistency between the RMS_{BA} as well as RMS_{ST-C} of the simulation and the real image data. For the analysis of the inner rings, the RMS_{BA} was 0.168 px without correction (M_1) and it was reduced to 0.057 px and 0.055 px with M_5 and M_8. The RMS_{BA} of the extended BA M_{10} was slightly higher with 0.067 px. The influence on the circle centers RMS_{ST-C} was also reduced to almost one third compared to M_1. The differences of the principle distances were smaller than in the simulation. There was a small reduction when applying the correction but the values were varying for the tests with the inner rings. The error reduction for the outer rings was even stronger due to the quadratic error behavior. The lowest RMS_{BA} was 0.092 px with M_9 and also RMS_{ST-C} was decreased to 0.07 mm. The differences of c were similar to the simulations. The correction with both rings M_7 reached a RMS_{BA} of 0.055 px and a RMS_{ST-C} of 0.07 mm. Thus, it was similar to the other methods. Thus, the simulation results were confirmed.

	RMS_{BA} in px	c in mm	RMS_{ST-C} in mm
M_1	0.168	12.17	0.17
M_2	0.646	12.29	0.61
M_3	0.098	12.14	0.08
M_4	0.341	12.17	0.10
M_5	0.057	12.15	0.07
M_6	0.111	12.17	0.07
M_7	0.055	12.14	0.07
M_8	0.055	12.15	0.07
M_9	0.092	12.17	0.07
M_{10}	0.067	12.16	0.07
M_{11}	0.120	12.14	0.07

Table 5. BA results of different models with 12 larger and 8 smaller concentric circles.

Just as with the simulation, the case of equal sized targets was considered by using only the first twelve targets of Table 1, see Table 6. For the inner rings, there was even a slight increase in RMS_{BA} and a slight reduction for the outer rings after application of the corrections. The estimated principle distances varied only slightly, making it difficult to see influences on the interior orientations. The RMS of the similarity transformations of the circle centers RMS_{ST-C} showed no significant changes. The results match the simulation, where also only small changes were computed for these three quantities. RMS_{ST-P} were not computed here due to the unknown target values of the exterior orientations, where larger deviations would be expected.

	RMS_{BA} in px	c in mm	RMS_{ST-C} in mm
M_1	0.048	12.13	0.08
M_2	0.076	12.11	0.08
M_3	0.052	12.13	0.08
M_4	0.060	12.09	0.08
M_5	0.054	12.15	0.08
M_6	0.074	12.17	0.08
M_7	0.056	12.14	0.08
M_8	0.053	12.15	0.07
M_9	0.063	12.17	0.07
M_{10}	0.074	12.16	0.08
M_{11}	0.125	12.12	0.07

Table 6. BA results of different models for the 12 larger equal sized concentric circles.

5. Scale Definition by Radii of Circles

As shown in Section 3.4, the radii of the circles are part of the model that can be introduced as unknowns or, secondly, can be used as constants as they are often known in practice. This means that they can also be used for the definition of the scale.

In order to investigate the precision and accuracy of the scale definition by given radii of circular targets, the experimental setup of Fig. 6 was used. A test field of coded and uncoded circular targets with radii of 5.0 mm was prepared. The radii were defined in a vector graphics software and printing errors were neglected. In order to check the distances, two scale bars with a higher accuracy were integrated at the edges of the test field: a horizontal one in the upper part of Fig. 6a and a vertical one in the right part of Fig. 6a. The radii of the scale bar target circles were measured with a slide gauge with 5.1 mm. A bundle of twelve images was recorded using a Nikon D300 camera and a Nikkor lens of 20 mm focal length with orientations as shown in Fig. 6b.

The experimental data was then processed using the algorithm of Section 3.4 with unknown radii and secondly with fixed radii. To evaluate the precision, the version with the unknown radii was analyzed. One parameter for the evaluation was the mean resulting standard deviation of the 212 estimated circle radii $mean(\sigma_{R,BA})$ from the stochastic model of the bundle adjustment (BA). Furthermore, the scattering of the 212 estimated circle radii (of the same target size) was expressed by the empirical standard deviation s_R that could be considered as a more representative precision quantity. Table 7 shows the results. Again, the RMS of the image ellipse center residual RMS_{BA} is depicted. Note that there was slight change in scale of the radii due to the free net adjustment with a scale condition so that the mean estimated radius was 5.014 mm instead of 5.000 mm. The relative precision was 0.0014.

RMS_{BA} in px	$mean(R)$ in mm	$mean(\sigma_{R,BA})$ in mm	s_R in mm	s_R/R
0.030	5.014	0.0045	0.0072	0.0014

Table 7. Precision analysis of the radii determination in the BA.

To evaluate the accuracy, the radii in the BA were fixed to define the scale and two scale bars were used to compare the estimated and the given distances. Note that there only six constraints of the free net adjustment were applied:

$$\sum_i d\vec{X}_{C,i} = \sum_i \vec{X}_{C,i} \times d\vec{X}_{C,i} = \vec{0} \tag{26}$$

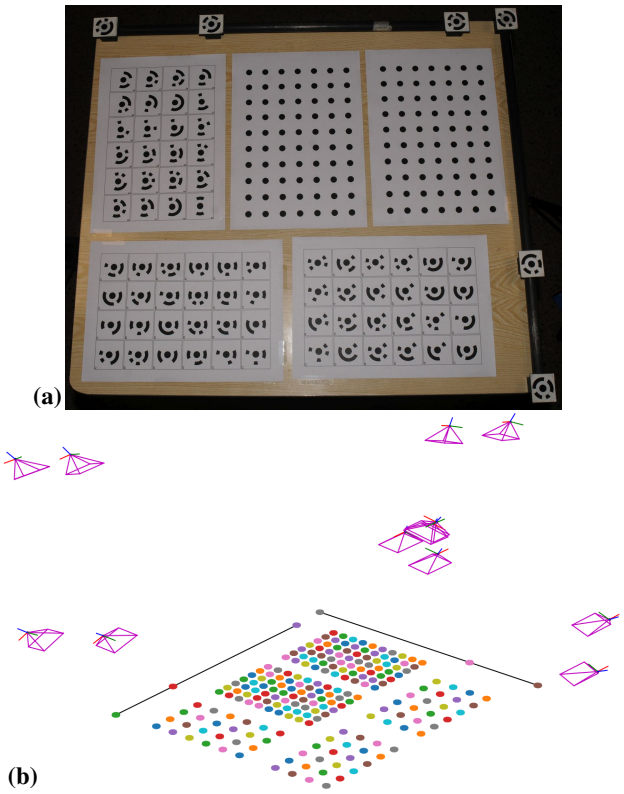

Figure 6. **(a)** test field with two scale bars; **(b)** image orientations, circles (targets) and two scale bars as black lines.

Table 8 reveals the results of the comparison of the distances of the two scale bars. The deviation was about 1 mm and the relative error was approximately two thousandths. The RMS_{BA} remained unchanged with 0.030 px.

	Scale bar 1	Scale bar 2
Target distance	576.210 mm	577.614 mm
Estimated distance	577.187 mm	578.627 mm
Deviation/difference	-0.977 mm	-1.013 mm
Relative error	0.0017	0.0018

Table 8. Accuracy analysis of the scale definition by radii.

The experiment showed that this method for scale definition is not suitable for high-accuracy measurements, but can be used for applications with lower accuracy requirements.

6. Conclusion

The article at hand shows different correction methods for the eccentricity effect of circular targets in perspective projection. The methods were tested in an experiment with a planar test field of concentric circles where the eccentricity reached values of up to 6 pixels. For the analysis of all targets with different sizes, the eccentricity error was verified by the RMS of the image residuals and similarity transformations of the circle centers. This error was strongly reduced by applying the corrections. When only equal sized targets were used, it was difficult to see influences and the effect of corrections due to correlations between target eccentricities and exterior orientation parameters.

The presented method of the extended bundle adjustment also offers the possibility of a scale definition by given target radii. This approach was tested in a further experiment where a relative accuracy of two thousandths (for a target radius to object dimension ratio of 1:115) was reached. The method is only suitable for applications with lower accuracy requirements. Future work could investigate the influence of the target size.

Acknowledgements

The research work was funded by the Deutsche Forschungsgemeinschaft (DFG, German Research Foundation – SFB/TRR 280; Projekt-ID: 417002380).

References

Ahn, S. J., Warnecke, H.-J., Kotowski, R., 1999. Systematic geometric image measurement errors of circular object targets: mathematical formulation and correction. *Photogramm. Rec.*, 16(93), 485–502.

Brown, Duane, C., 1971. Close-Range Camera Calibration. *Photogrammetric Engineering*, 37(8), 855–866.

Dold, J., 1996. Influence of Target Size on the Results of Photogrammetric Bundle Adjustment. *Int. Arch. Photogramm. Remote Sens. Spatial Inf. Sci.*, 31-B5, 119–123.

He, D., Liu, X., Yin, Y., Li, A., Peng, X., 2012. Correction of circular center deviation in perspective projection. A. G. Tescher (ed.), *Applications of Digital Image Processing XXXV*, 8499, International Society for Optics and Photonics, SPIE, 625–631.

Heikkilä, J., Silvén, O., 1997. A four-step camera calibration procedure with implicit image correction. *Proceedings of IEEE Computer Society Conference on Computer Vision and Pattern Recognition*, 1106–1112.

Kim, J.-S., Kim, H.-W., Kweon, I., 2002. A camera calibration method using concentric circles for vision applications. *Proceedings of ACCV2002: The 5th Asian Conference on Computer Vision, 23–25 January 2002, Melbourne, Australia*, 23–25.

Lenz, R., Fritsch, D., 1988. On the Accuracy of Videometry. *Int. Arch. Photogramm. Remote Sens. Spatial Inf. Sci.*, 27-B5, 335–345.

Luhmann, T., 2014. Eccentricity in images of circular and spherical targets and its impact on spatial intersection. *Photogramm. Rec.*, 29(148), 417–433.

Luhmann, T., Robson, S., Kyle, S., Boehm, J., 2020. *Close-Range Photogrammetry and 3D Imaging*. De Gruyter, Berlin, Boston.

Matsuoka, R., Maruyama, S., 2016. Eccentricity on an image caused by projection of a circle and a sphere. *ISPRS Ann. Photogramm. Remote Sens. Spatial Inf. Sci.*, 3(5), 19–26.

Otepka, J., Fraser, C., 2004. Accuracy Enhancement of Vision Metrology Through Automatic Target Plane Determination. *Int. Arch. Photogramm. Remote Sens. Spatial Inf. Sci.*, 35-B5, 873–879.

Wrobel, B. P., 2012. Kreismarken in perspektiver Abbildung – im Bild und im Bündelblock. *PFG - J. Photogramm. Remote Sens. Geoinf. Sci.*, 16(3), 221–236.